Towards Real-time Ion-specific Structural Sensitivity in Nanoporous Carbon Electrodes using In Situ Anomalous Small-angle X-ray Scattering

Christian Koczwara[1], Christian Prehal[1,2], Sylvio Haas[3], Peter Boesecke[4], Nicola Huesing[5], Oskar Paris[1,]*

1. Institute of Physics, Montanuniversitaet Leoben, Franz-Josef Straße 18, 8700 Leoben, Austria
2. Institute for Chemistry and Technology of Materials, Graz University of Technology, Stremayrgasse 9, 8010 Graz, Austria
3. Photon Science, DESY, Notkestraße 85, 22607 Hamburg, Germany
4. European Synchrotron Radiation Facility (ESRF), 6 Rue Jules Horowitz, BP 220, 38043 Grenoble, France
5. Chemistry and Physics of Materials, University of Salzburg, Jakob-Haringer Str. 2a, 5020 Salzburg, Austria

KEYWORDS: supercapacitor, EDLC, in situ, anomalous small-angle X-ray scattering, ion-specific, structural sensitivity

Abstract

Current in situ techniques to study ion charge storage and electrical double-layer formation in nanoporous electrodes are either chemically sensitive to element-specific concentration changes, or structurally sensitive to rearrangements of ions and solvent molecules; but rarely can they cover both. Here we introduce in situ anomalous small-angle X-ray scattering (ASAXS) as a unique method to extract both, real-time structural and ion-specific chemical information from one single experiment. Using a 1M RbBr aqueous electrolyte and a hierarchical micro- and mesoporous carbon electrode, we identify different charging mechanisms for positive and negative applied potentials. We are not only able to track the global concentration change of each ion species individually, but also to observe their individual local re-arrangement within the pore space.

Introduction

Ion electrosorption in the confined geometry of nanoporous carbons is the key process of capacitive energy storage in electrical double-layer capacitors[1,2] (EDLCs or supercapacitors) and seawater desalination via capacitive de-ionization[3] (CDI). The performance of both technologies ultimately depends on the way how ions counterbalance the electrode charge upon polarizing the carbon electrode.[1,4–6] During charging, the electronic charge can be counter-balanced either by counter-ion adsorption (adding counter-ions), by co-ion expulsion (removing co-ions) or by ion replacement (adding counter-ions and removing the same amount of co-ions).[1,3,7] CDI requires counter-ion adsorption, since only the total ion concentration increase in the nanopores leads to the decrease of the bulk electrolyte salt concentration. For EDLCs it is not clear at the moment which mechanism is desirable for highest energy and power densities.[8] Theoretical and experimental work could recently show how salt concentration, cell design, pore connectivity and cycling speed influence the electrosorption mechanism.[9–11] However, knowledge about material parameters that control the mechanisms on the atomic and nanoscale is still scarce. The most crucial requirement for further progress is hence a mechanistic understanding of processes taking place in the complex nanopore space: partial ion desolvation,[12–14] mutual ion blocking,[7,8] and local ion rearrangement into sites with highest degree of confinement.[12,15]

Answering these questions demands for real-time in situ experimental techniques that consider for the entire complexity of the nanopore structure,[16–18] and allow quantifying the ion electrosorption process. In recent years, a number of new electrochemical in situ techniques contributed towards this goal. Electrochemical quartz crystal microbalance (eQCM),[19] and in situ X-ray transmission (XRT)[10] can quantify the global cation and anion fluxes in and out of the carbon electrode upon charging and discharging. In situ small-angle X-ray scattering (SAXS) provides structural sensitivity on the length scale of micropores (i.e. pore size < 2nm) and mesopores (pore size between 2 nm and 50 nm),[20] and enables in principle the quantification of ion confinement, ion desolvation, local ion rearrangement across the carbon nanopores and mechanical strain of the carbon electrode.[12,21,22] Its combination with XRT permits covering both, local and global ion concentration changes from the same macroscopic sample volume.[21,23] However, neither eQCM, nor XRT / SAXS are specifically sensitive to the individual ions. All involved species like solvent molecules, cations, anions, and the carbon matrix contribute to the in situ signals and therefore, the necessary assumptions for data interpretation can potentially be ambiguous and over-simplified. Spectroscopic in situ

techniques like in situ nuclear magnetic resonance (NMR)[24–26] or in situ X-ray absorption spectroscopy[27] on the other hand are element-specific and can be used to quantify concentration changes of specific ions or molecules in operating devices.

Here we present in situ anomalous small-angle X-ray scattering (in situ ASAXS) as a powerful approach that fully utilizes the advantages of SAXS, and at the same time eliminates its main drawback concerning the lack of element sensitivity. In situ ASAXS provides simultaneous real-time structural and chemical information by combining SAXS with the principle of absorption spectroscopy by utilizing the change of the scattering power of a resonant element near its adsorption edge. We perform a proof-of-principle ASAXS experiment using a hierarchically porous carbon material with aqueous RbBr electrolyte that corroborates direct discrimination between different charging mechanisms - ion replacement versus co-ion repulsion - in a single experiment. The inherent nanometer spatial resolution of SAXS further allows sensing the ion specific local re-arrangements upon charging and discharging.

Experimental section

Material: Electrodes were produced from a monolithic carbon material with hierarchical porosity obtained from a nanocasting approach. The material consists of a macroporous network of struts, with each strut being composed of a hexagonal arrangement of carbon nanorods leaving mesopores in between the nanorods (Figure 1).

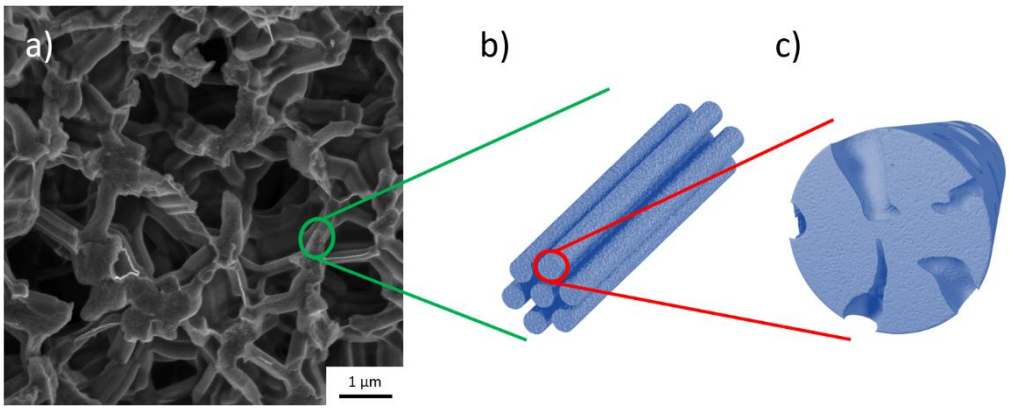

Figure 1: Schematic representation of the hierarchy of the ordered mesoporous carbon material. SEM image of the macropore structure (a); a schematic representation of the ordered nanorods with mesopores between them (b); schematic representation of one nanorod containing micropores (c).

The material was further activated to create micropores within the carbon nanorods. We do not have a detailed structural picture about these micropores, but we can expect them to predominantly create an increasing roughness of the nanorod surface with activation. Synthesis and characterization of the material was described already in earlier work.[22,28] Important parameters of the used sample are present in Table 1.

Table 1: Used nanocast carbon sample

Activation time[(a)] (h)	S_{DFT} [(b)] ($m^2\ g^{-1}$)	V_{micro} [(c)] ($cm^3\ g^{-1}$)	V_{meso} [(c)] ($cm^3\ g^{-1}$)	d_{50} (d_{25}-d_{75}) [(e)] (nm)	$C_{0.5}$ [(e)] ($F\ g^{-1}$)
2.0	1155	0.45	0.58	2.42 (1.26-3.07)	95

[(a)] CO_2 activation performed at 925 °C

[(b)] Specific surface area obtained from NL-DFT (S_{DFT}) from nitrogen adsorption isotherms at 77 K

[(c)] Specific micro- (pores < 2 nm) and mesopore volumes (pores between 2 nm and 50 nm)

[(d)] Volume-weighted median of the pore size d_{50} including the 25th and 75th percentile of the pore width (d_{25} and d_{75}),[29] see Figure S1 in the supporting information (SI)

[(d)] Specific capacitance obtained from cyclic voltammetry measurements using a scan rate of 0.5 mV s^{-1} and 1 M RbBr aqueous electrolyte (see Figure S2)

Electrode preparation: The monolithic carbon samples were ground to a fine powder and mixed with ethanol and a polytetrafluoroethylene (PTFE) dispersion (60% PTFE in water, Sigma-Aldrich) as a binder. The resulting slurry was rolled to an electrode with a thickness of 300 µm using a MSK-HRP-MR 100A (MTI Corporation) rolling press. The electrodes containing 10 mass% binder were then dried at 5 mbar and 120 °C for at least 24 hours. The supercapacitor had a sandwich like design and consisted of a working electrode (WE), a 300 µm thick glass filter (Whatman GF/A) as a separator, an oversized counter electrode (CE) as quasi reference,[30] and two platinum current collectors (CC). The CE was made of a commercially available activated carbon powder (YP-80F, Kuraray Chemicals) and contained a reduced amount (5 mass%) of PTFE binder.

In Situ ASAXS: In situ anomalous small-angle X-ray scattering (ASAXS) measurements were performed using a custom-made cell similar to the setup published by Ruch et al.[31] and to previous experiments.[12,21] The housing made of the polyether ether ketone (PEEK) and titanium was specifically designed for in situ SAXS measurements.[10,21–23] To guarantee that the scattering signal originates from the investigated WE only, a 3 mm diameter hole was punched in each component except the WE. In contrast to our previous experiments there was also a hole punched into the platinum CC foil, since Pt exhibits an absorption edge within the energy range used for the present experiment.[32] A 1M RbBr aqueous electrolyte was used.

The experiments were performed at the ID02 beamline at the European Synhrotron Radiation Facility (ESRF) in Grenoble, France.[33] 2D SAXS pattern were recorded with a MX 170 (Rayonix) detector. A photodiode mounted on the beamstop in front of the detector was used to measure the transmitted X-ray intensity after passing through the sample during the scattering experiments. Chronoamperometry measurements were performed at 0 V and ±0.6 V, using a Reference 600 Potentiostat (Gamry). 2D Scattering patterns were recorded at different energies near the absorption edges of Br (E=13474 eV) and Rb (E=15200 eV) for each applied voltage after an equilibration time of approximately 2000 s after each voltage step (Figure 2). After correcting the data for detector specific imperfections (dark image, flat field, distortion) the 2D scattering patterns were corrected for solid-angle effects, normalized to the recorded transmitted intensity and azimuthally averaged.[33,34] The energy depending efficiency of the detector was taken into account by normalizing it to the scattering intensity of an energy independent standard sample (glassy carbon).

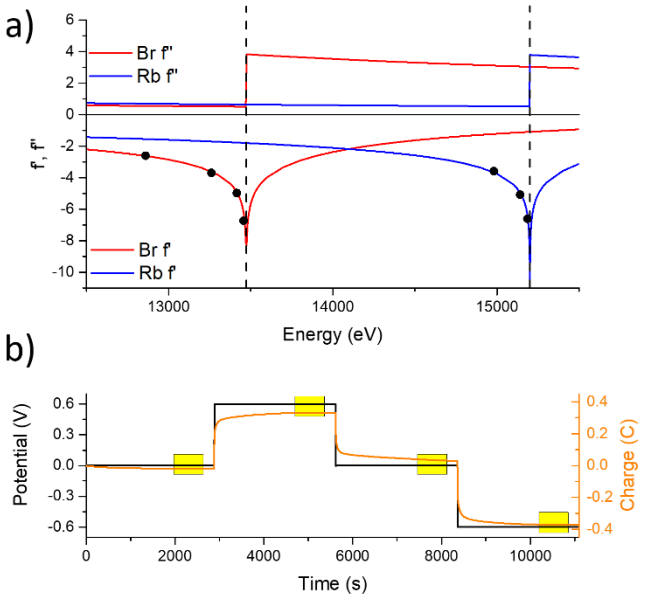

Figure 2: (a) Tabulated real- (f') and imaginary (f'') parts of the energy dependent anomalous scattering factors as a function of the photon energy for Br and Rb.[32] The vertical dashed lines mark the absorption edges (Br: 13474 eV; Rb: 15200 eV) and the black dots are the energies where ASAXS experiments were performed. (b) Chronoamperometry measurements with the yellow boxes indicating the time period needed to perform the ASAXS measurements at the 7 different energies marked in (a). The accumulated charge for positive applied potential is lower than for negative potential (orange curve in b). This is consistent with CV measurements (Figure S2).

Data evaluation: The effective scattering strength of an ion (i.e., the probability that an X-ray photon is scattered by the ion) is proportional to its atomic scattering factor *f*. ASAXS utilizes the fact that f strongly varies with X-ray energy near an absorption edge of the ion [35,36]

$$f(E) = f_0 + f'(E) + if''(E) \quad (1)$$

For small scattering angles, the energy independent term f_0 is simply given by the number of electrons in the atom or ion, and $f'(E)$ and $f''(E)$ are the real and imaginary parts of the energy dependent anomalous scattering factor[37,38] (Figure 2a). The imaginary part f'' is related to the X-ray absorption coefficient and is essentially constant at energies below the absorption edges (dashed vertical lines). The effective number of electrons of the resonant ion is however reduced in this region. Consequently, several SAXS measurements at different photon energies

below the absorption edge of the resonating ion (black circles in Figure 2a) allow to change its effective electron number by a controlled extent (at maximum by roughly 10% considering Br^- and Rb^+ having the same number of electrons, $f_0 = 36$). The total SAXS amplitude of the sample can be generally written as the sum of a non-resonant and a resonant contribution, and since the SAXS intensity is the absolute square of the amplitude:[35]

$$I(q) = F_0^2(q) + 2f'(E)F_0(q)F_R(q) + (f'(E)^2 + f''(E)^2)F_R^2(q) \quad (2)$$

where F_0 and F_R are the non-resonant and resonant amplitudes, respectively.

The separation of the non-resonant and the resonant scattering contribution in Eq. 2 can be performed by using a quadratic fit (described in the SI) considering that in the chosen energy range $(f'')^2 << (f')^2$ (see Figure 2a)[39] or by solving a linear system of equations:[40] A set of n SAXS measurements at different energies E_i results in a set of n linear equations from Eq. 2:[40,41]

$$\begin{bmatrix} 1 & 2f'(E_1) & (f'(E_1)^2 + f''(E_1)^2) \\ \vdots & \vdots & \vdots \\ 1 & 2f'(E_n) & (f'(E_n)^2 + f''(E_n)^2) \end{bmatrix} \cdot \begin{bmatrix} {F_0}^2(q_i) \\ F_0(q_i)F_R(q_i) \\ {F_R}^2(q_i) \end{bmatrix} = \begin{bmatrix} I(E_1, q_i) \\ \vdots \\ I(E_n, q_i) \end{bmatrix} \quad (3)$$

By solving this set of linear equations for all measured q_i -values, the non-resonant (${F_0}^2$) and the resonant (${F_R}^2$) scattering intensities as well as the mixed (F_0F_R) term can be obtained. The for the data separation needed values of f' and f'' can be influenced by instrumental and chemical shifts, which also has to be taken into account for the data evaluation (see SI).

For energies below the Br edge, the absence of any (energy dependent) fluorescence radiation allows a straight forward separation of the three scattering contributions using Eq. 3. The calculation of the resonant scattering curve was performed by using all four energies as well as each possible subset of three different energies and the set of all four resonant curves was averaged.

The fact that the Rb edge is quite close to the Br absorption edge leads to a significant contribution of Br-fluorescence for the ASAXS experiments at the Rb edge, as shown Figure S4. This additional q-independent, but energy dependent contribution in the SAXS data can dramatically change the calculated resonant scattering contribution. The voltage dependent scattering intensity from anion and cation concentration changes, together with the unknown voltage and energy dependent fluorescence from Br^- ions in the electrode prevents an exact solution of Eq. 3 particularly for large q values.[36] The influence of the fluorescence is discussed in more detail in the SI.

Results and discussion

The SAXS data at a given energy far from both adsorption edges (Figure 3a) show an overall increase of the intensity at +0.6V and a decrease at -0.6 V as compared to the neutral case at 0 V, with q-dependent detailed changes. If we recall that Br^- and Rb^+ have the same number of electrons ($f_0 = 36$), and the anomalous contributions (Eq. 1) are small at this energy, a pure ion replacement mechanism is not compatible with these changes. The SAXS experiments at different energies (Figure 3b) show a small but systematic dependency of the scattering intensity on the photon energy.

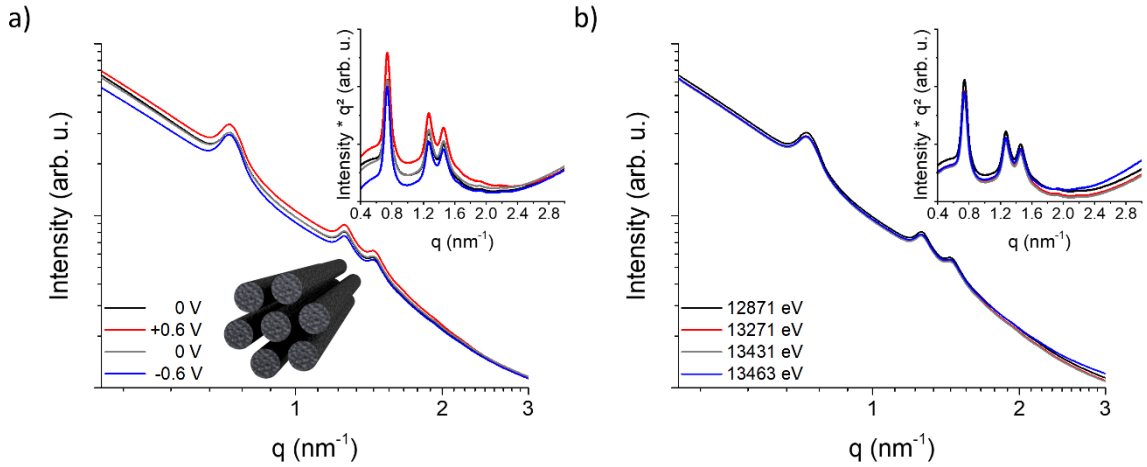

Figure 3: SAXS intensity profiles from the working electrode at different applied potentials and a photon energy of 12871 eV (a), and at different photon energies close to the Br^- edge at a potential of 0 V (b). For a better visualization of the Bragg peaks from the hexagonally ordered carbon nanorods (schematically shown in (a)), the insets show so called Kratky plots[42] $I(q)q^2$ versus q, with the area under these profiles representing the integrated intensity

The separated, non-resonant scattering intensity (Figure 4a black line) contains the usual SAXS information from all species within the irradiated volume, similar to the curves in Figure 3a. The resonant scattering curve (Figure 4a, red curve) contains information on the spatial arrangement of the resonant ion (Br^- in this case) only, as illustrated schematically in the corresponding inset.

First, we note that the magnitude of the resonant term is about two orders of magnitude smaller than the one of the non-resonant term, which gives an indication of the high demands on data quality and statistical accuracy for ASAXS experiments. Second, we recognize that the shapes of the resonant and non-resonant scattering curves are rather similar. Therefore, we

concentrate first on the total (integrated) intensity changes of the resonant scattering curves with applied potential. For Br^- (Figure 4b) they show a significantly stronger intensity decrease for negative potential (-0.6 V) as compared to the intensity increase for positive potential (+0.6 V). The second (control) measurement at 0 V shows only minor intensity changes (see SI for more details). Unfortunately, at the Rb edge, the data analysis of the energy dependent SAXS signal is more problematic due to an additional X-ray fluorescence term originating from the Br^- ions, and a slight change also of the anomalous *f'* contribution from Br^- (see Figure 2a).[43] The resonant and non-resonant ASAXS contributions from the Rb edge could still be separated assuming f'_{Br} and the fluorescence contribution to be approximately constant in the chosen energy interval. As a result, the resonant ASAXS curves from the Rb-edge (see SI for detailed data evaluation and fluorescence separation) are considerably more noisy as compared to those from the Br-edge. Yet, a noteworthy different change of the resonant Rb^+ scattering curves with the applied potential is obvious in Figure 4c. The intensity increases for negative and decreases for positive potential in this case as expected, but in contrast to Br^-, there is no evident asymmetry with respect to 0 V for Rb^+.

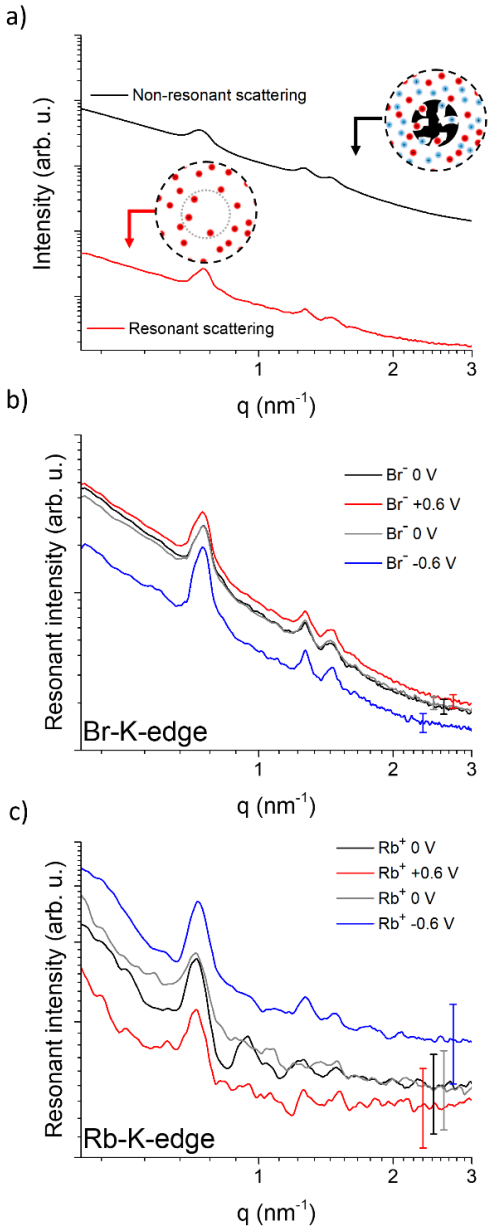

Figure 4: (a) Non-resonant (black) and resonant (red) ASAXS intensity obtained from the Br edge at a potential of 0 V. The insets show schematically the contributing scattering species within the micropores in a carbon nanorod and in the adjacent mesopore (black: carbon; red: Br^-; blue: Rb^+; the solvent water also contributes to the non-resonant scattering, but is not shown for clarity). (b) and (c) show the resonant ASAXS intensity profiles for the Br- and the Rb edges, respectively, for the different applied potentials. A significantly higher uncertainty in (c) compared to (b) is the result of the fluorescence contribution and the reduced amount of energies used for separation (see SI).

The integrated intensity $\tilde{I} = \int q^2 I(q)\, dq$ of a two-phase system (e.g. pores in carbon) is proportional to $\phi(1-\phi)\Delta\rho^2$, where ϕ is the porosity and $\Delta\rho^2$ the effective electron density contrast between pores and carbon.[42] Similarly, for the resonant scattering curves, the mean effective electron density level in the pores is determined by the concentration of the corresponding resonant ion species. Assuming negligible (effective) porosity changes,[21] the square root of the integrated intensity change is therefore proportional to the resonant ion concentration change (Figure 5a). The amount of Br^- ions is higher and the amount of Rb^+ ions is lower at positive potential as compared to 0 V, and the opposite holds true for negative potential. Interestingly, the Br^- ions clearly show a different behavior for positive and negative potentials. At positive potential, the concentration of anions increases slightly, while it is significantly reduced at negative potential. In contrast, the behavior of the cations (Rb^+) appears to be symmetric around 0 V. We stress again that the data for the Rb^+ ions show a considerably larger experimental uncertainty than the Br^- data, and a possible slight asymmetry for the cations cannot unambiguously be excluded. Yet, the data in Figure 5a suggest that there are two different charging mechanisms present, depending on the applied potential: ion replacement for negative applied potential, and a combination of co-ion expulsion and ion replacement for positive potential. Interestingly, the asymmetry in the cation and anion concentration changes goes along with a slight asymmetry in the observed specific capacitance (Figure S2). Co-ion expulsion has recently been observed in electrodes with organic electrolyte using in situ NMR,[24] and in the initial state of charging in disordered activated carbon electrodes with aqueous RbBr using in situ XRT.[10] We consider two possible reasons for the observed behavior. First, differences in ion size (bare and hydrated), hydration enthalpy, or mobility[7,10] (Table 2), might cause ion-specific interactions with the carbon confinement and thus asymmetric concentration changes. Second, specifically adsorbed Br^- ions at 0V, possibly cause a negative potential of zero charge, resulting in a saturation of adsorbed Br ions at positive potentials.[44,45] The data given in Figure 5a do not directly contain this information, since only the relative intensity change with respect to the intensity at 0V is given. Detailed atomistic simulations and additional experiments are needed to fully understand the origin of the different ion behavior, which is beyond the scope of this work.

Table 2: Ion radii and mobility in water, as well as the hydration enthalpy

Ion	Bare ion radius[46] (nm)	Hydrated radius[46] (nm)	Mobility[47] (10^{-8} m^2 V^{-1} s^{-1})	Diffusion coefficient[47] (10^{-9} m^2 s^{-1})	Hydration enthalpy[2] (kJ mol^{-1})
Br^-	0.195	0.330	7.20	1.85	-17.9
Rb^+	0.148	0.329	7.70	1.98	-18.5

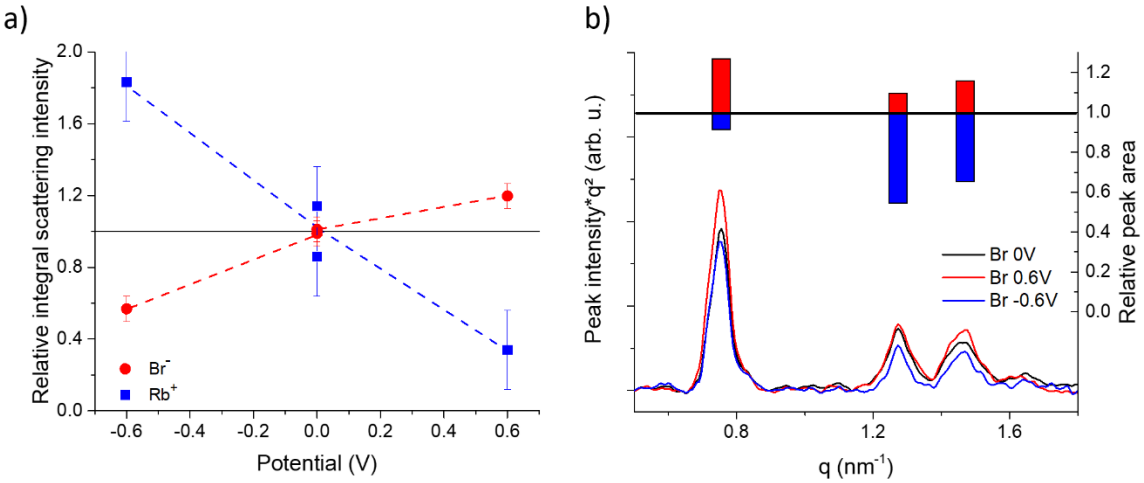

Figure 5: (a) Integrated intensity of the resonant scattering curves versus applied potential for Rb+ (blue) and Br- (red). The dashed lines are guides for the eye. (b) Kratky plot of the Bragg-peaks (after subtraction of the diffuse scattering) and relative peak area for different applied potentials for the resonant Br-curves. The bars are drawn to better visualize the different changes of the area of the three Bragg peaks with applied potential, calculated from the Kratky plot at +0.6 V (red) and -0.6 V (blue) relative to 0 V.

The integrated intensity provides information on the element-specific cation and anion concentration changes within the range of length scales covered by the q-range in the SAXS data ($\pi/q \approx$ 1 nm – 7 nm). Since this range covers essentially the entire range of micro- and mesopore sizes of the investigated carbon (Figure 1), we interpret these changes as *global ion concentration* changes. Additional information on possible *local ion-specific re-*

arrangement[12,21,23] may be obtained from the q-dependent changes of the resonant SAXS profiles. We restrict the following discussion to the anions only, because of the large scatter of the resonant scattering data from the Rb edge. While the diffuse scattering in Figure 4b does not exhibit noticeable q-dependent intensity variations, the three Bragg reflections from the ordered mesopore arrangement do show peak-dependent changes with the applied potential. This is visualized in Figure 5b, where the diffuse scattering contribution was subtracted from each resonant Br^- SAXS profile. We observe a similar trend as for the integrated intensity, i.e., a peak intensity decrease for negative potential and an increase for positive potential. However, there are obvious differences for the three Bragg peaks as indicated by the relative Bragg-peak areas in Figure 5b. The first order Bragg-peak decrease at negative potential is less than the increase at positive potential, just opposite to the integrated intensity (Figure 5a). This is a clear sign of a local redistribution of the Br^- ions. Indeed, such diffraction-peak intensity changes are known to be very sensitive to the form-factor of the ordered mesopore structure, which is affected by the adsorption of guest species at or within the mesopore walls.[48] A future quantification attempt requires detailed information on the nanopore structure (such as the activation induced microporosity gradient within the carbon nanorods), and sufficiently large changes of the Bragg-peaks to set-up a detailed form-factor model. The ASAXS capabilities of element specificity, together with improved model carbons with more clearly separated micro- and mesopore distributions, can thus enable unimagined details of ion re-arrangement in hierarchical pore spaces. We emphasize that compared to previous in situ SAXS studies,[10,12,21,23] no additional electrochemical data are necessary for in situ ASAXS, as it is both, structure- and element sensitive. This fact may not be of academic interest only, as electrochemical data include the whole electrode, while the SAXS (and XRT) measurements cover typically a much smaller electrode volume hit by the X-ray beam. Therefore, such experiments would enable also position sensitive ASAXS measurements at different electrode locations, and would for instance allow studying the influence of the cell design on the local ion storage mechanism.

Conclusion

In conclusion, we have shown that in situ ASAXS is a powerful new method providing access to real-time ion-specific structural information in an aqueous nanoporous carbon-based supercapacitor cell. Different relative global- and local concentration changes of anions and cations were shown to occur for positive and negative applied potentials in an activated carbon

electrode with ordered mesopores. This proof-of-principle experiment sets the basis to exploit the full potential of in situ ASAXS for contributing to the elucidation of further unknown details of ion electrosorption in nanoporous carbons. For instance, the recent advanced SAXS data analysis method to synergistically combine SAXS with atomistic Monte Carlo simulations[12,23] can easily be extended to element-specific ASAXS. ASAXS might also prove useful to unambiguously separate intensity changes due to the local ion re-arrangement within the pores from the concomitant ion electrosorption-induced volume changes of the pore space.[22] More generally, the lack of suitable structure-sensitive in situ techniques critically impedes progress in increasingly complex electrochemical systems for energy storage and conversion beyond supercapacitors and CDI. In situ ASAXS has the potential to contribute substantially to fill this gap in the future. However, its future widespread use relies on highest data quality, further experimental and theoretical development, a wide accessible energy range, and access to specialized beamlines dedicated for ASAXS.

ASSOCIATED CONTENT

The following files are available free of charge.
Supporting Information (PDF) containing gas adsorption data electrochemical data and additional description of ASAXS analysis

AUTHOR INFORMATION

Corresponding Author

* Corresponding author: Oskar Paris (oskar.paris@unileoben.ac.at)

Author Contributions

C.K. and O.P. performed the ASAXS experiment. P.B. supported the ASAXS experiments at ESRF. S.H. supported the data analysis. C.K., C.P., O.P. and N.H. conceptualized the work. . C.K., C.P., O.P. interpreted the data and wrote the manuscript. All authors have given approval to the final version of the manuscript.

Funding Sources

Funding of this research was provided by the Austrian Klima- und Energiefonds via the FFG programme “Energieforschung” (Project: Hybrid Supercap, Project Number: 848808).

ACKNOWLEDGMENT

We acknowledge financial support from the Austrian Klima und Energiefonds via the FFG program "Energieforschung" (project Hybrid Supercap, project no. 848808), and the European Synchrotron Radiation Facility ESRF (Grenoble, France) for providing beam time. We are grateful to M. Stzucki and T. Narayanan for help at the beamline. CP thanks Stefan Freunberger for discussions and continuing support.

ABBREVIATIONS

ASAXS, anomalous small-angle X-ray scattering; SAXS, small-angle X-ray scattering; NMR, nuclear magnetic resonance; EDLC, electrical double-layer capacitors; CDI, capacitive de-ionization; eQCM, electrochemical quartz crystal microbalance; XRT, X-ray transmission; SI, supporting information

REFERENCES

(1) Salanne, M.; Rotenberg, B.; Naoi, K.; Kaneko, K.; Taberna, P.-L.; Grey, C. P.; Dunn, B.; Simon, P. Efficient Storage Mechanisms for Building Better Supercapacitors. *Nat. Energy* **2016**, *1*, 16070, DOI: 10.1038/nenergy.2016.70.

(2) *Supercapacitors: Materials, Systems, and Applications;* Beguin, F.; Frackowiak, E., Eds.; Materials for Sustainable Energy and Development; Wiley: Weinheim, 2013.

(3) Suss, M. E.; Porada, S.; Sun, X.; Biesheuvel, P. M.; Yoon, J.; Presser, V. Water Desalination via Capacitive Deionization: What is it and what can we expect from it? *Energy Environ. Sci.* **2015**, *8*, 2296–2319, DOI: 10.1039/c5ee00519a.

(4) Simon, P.; Gogotsi, Y. Materials for Electrochemical Capacitors. *Nat. Mater.* **2008**, *7*, 845–854, DOI: 10.1038/nmat2297.

(5) Beguin, F.; Presser, V.; Balducci, A.; Frackowiak, E. Carbons and Electrolytes for Advanced Supercapacitors. *Adv. Mater. (Weinheim, Ger.)* **2014**, *26*, 2219-51, 2283, DOI: 10.1002/adma.201304137.

(6) Porada, S.; Zhao, R.; van der Wal, A.; Presser, V.; Biesheuvel, P. M. Review on the Science and Technology of Water Desalination by Capacitive Deionization. *Progress in Materials Science* **2013**, *58*, 1388–1442, DOI: 10.1016/j.pmatsci.2013.03.005.

(7) Forse, A. C.; Griffin, J. M.; Merlet, C.; Carretero-Gonzalez, J.; Raji, A.-R. O.; Trease, N. M.; Grey, C. P. Direct Observation of Ion Dynamics in Supercapacitor Electrodes using In Situ Diffusion NMR Spectroscopy. *Nat. Energy* **2017**, *2*, 1760, DOI: 10.1038/nenergy.2016.216.

(8) Kondrat, S.; Wu, P.; Qiao, R.; Kornyshev, A. A. Accelerating Charging Dynamics in Subnanometer Pores. *Nat. Mater.* **2014**, *13*, 387–393, DOI: 10.1038/nmat3916.

(9) Vasilyev, O. A.; Kornyshev, A. A.; Kondrat, S. Connections Matter: On the Importance of Pore Percolation for Nanoporous Supercapacitors. *ACS Appl. Energy Mater.* **2019,** DOI: 10.1021/acsaem.9b01069.

(10) Prehal, C.; Koczwara, C.; Amenitsch, H.; Presser, V.; Paris, O. Salt Concentration and Charging Velocity Determine Ion Charge Storage Mechanism in Nanoporous Supercapacitors. *Nat. Commun.* **2018**, *9*, 4145, DOI: 10.1038/s41467-018-06612-4.

(11) Biesheuvel, P. M.; Porada, S.; Levi, M.; Bazant, M. Z. Attractive Forces in Microporous Carbon Electrodes for Capacitive Deionization. *J Solid State Electrochem* **2014**, *18*, 1365–1376, DOI: 10.1007/s10008-014-2383-5.

(12) Prehal, C.; Koczwara, C.; Jäckel, N.; Schreiber, A.; Burian, M.; Amenitsch, H.; Hartmann, M. A.; Presser, V.; Paris, O. Quantification of Ion Confinement and Desolvation in Nanoporous Carbon Supercapacitors with Modelling and In Situ X-ray Scattering. *Nat. Energy* **2017**, *2*, 16215, DOI: 10.1038/nenergy.2016.215.

(13) Chmiola, J.; Largeot, C.; Taberna, P.-L.; Simon, P.; Gogotsi, Y. Desolvation of Ions in Subnanometer Pores and its Effect on Capacitance and Double-layer Theory. *Angewandte Chemie (International ed. in English)* **2008**, *47*, 3392–3395, DOI: 10.1002/anie.200704894.

(14) Levi, M. D.; Levy, N.; Sigalov, S.; Salitra, G.; Aurbach, D.; Maier, J. Electrochemical Quartz Crystal Microbalance (EQCM) Studies of Ions and Solvents Insertion into Highly Porous Activated Carbons. *J. Am. Chem. Soc.* **2010**, *132*, 13220–13222, DOI: 10.1021/ja104391g.

(15) Merlet, C.; Pean, C.; Rotenberg, B.; Madden, P. A.; Daffos, B.; Taberna, P.-L.; Simon, P.; Salanne, M. Highly Confined Ions Store Charge More Efficiently in Supercapacitors. *Nat. Commun.* **2013**, *4,* DOI: 10.1038/ncomms3701.

(16) Prehal, C.; Grätz, S.; Krüner, B.; Thommes, M.; Borchardt, L.; Presser, V.; Paris, O. Comparing Pore Structure Models of Nanoporous Carbons Obtained from Small Angle X-ray scattering and gas adsorption. *Carbon* **2019**, *152*, 416–423, DOI: 10.1016/j.carbon.2019.06.008.

(17) Jäckel, N.; Rodner, M.; Schreiber, A.; Jeongwook, J.; Zeiger, M.; Aslan, M.; Weingarth, D.; Presser, V. Anomalous or Regular Capacitance? The Influence of Pore Size Dispersity on Double-layer Formation. *J. Power Sources* **2016**, *326*, 660–671, DOI: 10.1016/j.jpowsour.2016.03.015.

(18) Chmiola, J.; Yushin, G.; Gogotsi, Y.; Portet, C.; Simon, P.; Taberna, P. L. Anomalous Increase in Carbon Capacitance at Pore Sizes Less than 1 Nanometer. *Science* **2006**, *313*, 1760–1763, DOI: 10.1126/science.1132195.

(19) Levi, M. D.; Salitra, G.; Levy, N.; Aurbach, D.; Maier, J. Application of a Quartz-crystal Microbalance to Measure Ionic Fluxes in Microporous Carbons for Energy Storage. *Nat. Mater.* **2009**, *8*, 872–875, DOI: 10.1038/nmat2559.

(20) Thommes, M.; Kaneko, K.; Neimark, A. V.; Olivier, J. P.; Rodriguez-Reinoso, F.; Rouquerol, J.; Sing, K. S.W. Physisorption of Gases, with Special Reference to the Evaluation of Surface Area and Pore Size Distribution (IUPAC Technical Report). *Pure and Applied Chemistry* **2015**, *87*, 160, DOI: 10.1515/pac-2014-1117.

(21) Prehal, C.; Weingarth, D.; Perre, E.; Lechner, R. T.; Amenitsch, H.; Paris, O.; Presser, V. Tracking the Structural Arrangement of Ions in Carbon Supercapacitor Nanopores using In Situ Small-angle X-ray Scattering. *Energy Environ. Sci.* **2015**, *8*, 1725–1735, DOI: 10.1039/c5ee00488h.

(22) Koczwara, C.; Rumswinkel, S.; Prehal, C.; Jäckel, N.; Elsässer, M. S.; Amenitsch, H.; Presser, V.; Hüsing, N.; Paris, O. In Situ Measurement of Electrosorption-Induced Deformation Reveals the Importance of Micropores in Hierarchical Carbons. *ACS Appl. Mater. Interfaces* **2017**, *9*, 23319–23324, DOI: 10.1021/acsami.7b07058.

(23) Prehal, C.; Koczwara, C.; Jäckel, N.; Amenitsch, H.; Presser, V.; Paris, O. A Carbon Nanopore Model to Quantify Structure and Kinetics of Ion Electrosorption with In Situ Small-angle X-ray Scattering. *Phys. Chem. Chem. Phys.* **2017**, *19*, 15549–15561, DOI: 10.1039/c7cp00736a.

(24) Griffin, J. M.; Forse, A. C.; Tsai, W.-Y.; Taberna, P.-L.; Simon, P.; Grey, C. P. In Situ NMR and Electrochemical Quartz Crystal Microbalance Techniques Reveal the Structure of the Electrical Double Layer in Supercapacitors. *Nat. Mater.* **2015**, *14*, 812–819, DOI: 10.1038/NMAT4318.

(25) Griffin, J. M.; Forse, A. C.; Wang, H.; Trease, N. M.; Taberna, P.-L.; Simon, P.; Grey, C. P. Ion Counting in Supercapacitor Electrodes using NMR Spectroscopy. *Faraday discussions* **2014**, *176*, 49–68, DOI: 10.1039/c4fd00138a.

(26) Borchardt, L.; Oschatz, M.; Paasch, S.; Kaskel, S.; Brunner, E. Interaction of Electrolyte Molecules with Carbon Materials of Well-defined Porosity: Characterization by Solid-state NMR Spectroscopy. *Phys. Chem. Chem. Phys.* **2013**, *15*, 15177–15184, DOI: 10.1039/C3CP52283K.

(27) Aquilanti, G.; Giorgetti, M.; Dominko, R.; Stievano, L.; Arčon, I.; Novello, N.; Olivi, L. Operando Characterization of Batteries using X-ray Absorption Spectroscopy: Advances at the Beamline XAFS at Synchrotron Elettra. *J. Phys. D: Appl. Phys.* **2017**, *50*, 74001, DOI: 10.1088/1361-6463/aa519a.

(28) Koczwara, C.; Rumswinkel, S.; Hammerschmidt, L.; Salihovic, M.; Elsaesser, M. S.; Amenitsch, H.; Paris, O.; Huesing, N. Nanofibers versus Nanopores: A Comparison of the Electrochemical Performance of Hierarchically Ordered Porous Carbons. *ACS Appl. Energy Mater.* **2019**, *2*, 5279–5291, DOI: 10.1021/acsaem.9b01035.

(29) Jäckel, N.; Simon, P.; Gogotsi, Y.; Presser, V. Increase in Capacitance by Subnanometer Pores in Carbon. *ACS Energy Lett.* **2016**, *1*, 1262–1265, DOI: 10.1021/acsenergylett.6b00516.

(30) Lee, J.; Jäckel, N.; Kim, D.; Widmaier, M.; Sathyamoorthi, S.; Srimuk, P.; Kim, C.; Fleischmann, S.; Zeiger, M.; Presser, V. Porous Carbon as a Quasi-reference Electrode in Aqueous Electrolytes. *Electrochim. Acta* **2016**, *222*, 1800–1805, DOI: 10.1016/j.electacta.2016.11.148.

(31) Ruch, P. W.; Hahn, M.; Cericola, D.; Menzel, A.; Kötz, R.; Wokaun, A. A Dilatometric and Small-angle X-ray Scattering Study of the Electrochemical Activation of Mesophase Pitch-derived Carbon in Non-aqueous Electrolyte Solution. *Carbon* **2010**, *48*, 1880–1888, DOI: 10.1016/j.carbon.2010.01.032.

(32) Brennan, S.; Cowan, P. L. A Suite of Programs for Calculating X-ray Absorption, Reflection, and Diffraction Performance for a Variety of Materials at Arbitrary Wavelengths. *Review of Scientific Instruments* **1992**, *63*, 850–853, DOI: 10.1063/1.1142625.

(33) Narayanan, T.; Sztucki, M.; van Vaerenbergh, P.; Léonardon, J.; Gorini, J.; Claustre, L.; Sever, F.; Morse, J.; Boesecke, P. A Multipurpose Instrument for Time-resolved Ultra-small-angle and Coherent X-ray Scattering. *J. Appl. Crystallogr.* **2018**, *51*, 1511–1524, DOI: 10.1107/S1600576718012748.

(34) Boesecke, P. Reduction of Two-dimensional Small- and Wide-angle X-ray Scattering data. *J. Appl. Crystallogr.* **2007**, *40*, s423-s427, DOI: 10.1107/S0021889807001100.

(35) Stuhrmann, H. B. Resonance Scattering in Macromolecular Structure Research. In *Characterization of Polymers in the Solid State II: Synchrotron Radiation, X-ray Scattering and Electron Microscopy*; Kausch, H. H., Zachmann, H. G., Eds.; Advances in Polymer Science 67; Springer: Berlin, Heidelberg, 1985; pp 123–163.

(36) Haas, S.; Hoell, A.; Wurth, R.; Rüssel, C.; Boesecke, P.; Vainio, U. Analysis of Nanostructure and Nanochemistry by ASAXS: Accessing Phase Composition of Oxyfluoride Glass Ceramics Doped with Er3+/Yb3+. *Phys. Rev. B* **2010**, *81*, 161, DOI: 10.1103/PhysRevB.81.184207.

(37) Dingenouts, N.; Merkle, R.; Guo, X.; Narayanan, T.; Goerigk, G.; Ballauff, M. Use of Anomalous Small-angle X-ray Scattering for the Investigation of Highly Charged Colloids. *J. Appl. Crystallogr.* **2003**, *36*, 578–582, DOI: 10.1107/S0021889803000256.

(38) Dingenouts, N.; Patel, M.; Rosenfeldt, S.; Pontoni, D.; Narayanan, T.; Ballauff, M. Counterion Distribution around a Spherical Polyelectrolyte Brush Probed by Anomalous Small-angle X-ray Scattering. *Macromolecules* **2004**, *37*, 8152–8159, DOI: 10.1021/ma048828j.

(39) Ballauff, M.; Jusufi, A. Anomalous Small-angle X-ray Scattering: Analyzing Correlations and Fluctuations in Polyelectrolytes. *Colloid and polymer science* **2006**, *284*, 1303–1311, DOI: 10.1007/s00396-006-1516-5.

(40) Sztucki, M.; Cola, E.; Narayanan, T. Anomalous Small-angle X-ray Scattering from Charged Soft Matter. *The European Physical Journal Special Topics* **2012**, *208*, 319–331, DOI: 10.1140/epjst/e2012-01627-x.

(41) Sztucki, M.; Di Cola, E.; Narayanan, T. Instrumental Developments for Anomalous Small-angle X-ray Scattering from Soft Matter Systems. *J. Appl. Crystallogr.* **2010**, *43*, 1479–1487, DOI: 10.1107/S002188981003298X.

(42) *Small angle X-ray scattering;* Glatter, O.; Kratky, O., Eds.; Acad. Pr: London, 1982.

(43) Sztucki, M.; Di Cola, E.; Narayanan, T. New Opportunities for Anomalous Small-Angle X-Ray Scattering to Characterize Charged Soft Matter Systems; p 12004.

(44) Golub, D.; Oren, Y.; Soffer, A. Electro Adsorption, the Electrical Double Layer and their Relation to Dimensional Changes of Carbon Electrodes. *Carbon* **1987**, *25*, 109–117, DOI: 10.1016/0008-6223(87)90047-9.

(45) Kosmulski, M. *Surface Charging and Points of Zero Charge*; CRC Press, 2009.

(46) Nightingale, E. R. Phenomenological Theory of Ion Solvation. Effective Radii of Hydrated Ions. *J. Phys. Chem.* **1959**, *63*, 1381–1387, DOI: 10.1021/j150579a011.

(47) Koneshan, S.; Rasaiah, J. C.; Lynden-Bell, R. M.; Lee, S. H. Solvent Structure, Dynamics, and Ion Mobility in Aqueous Solutions at 25 °C. *J. Phys. Chem. B* **1998**, *102*, 4193–4204, DOI: 10.1021/jp980642x.

(48) Zickler, G. A.; Jähnert, S.; Wagermaier, W.; Funari, S. S.; Findenegg, G. H.; Paris, O. Physisorbed Films in Periodic Mesoporous Silica Studied by In Situ Synchrotron Small-angle Diffraction. *Phys. Rev. B* **2006**, *73*, 17, DOI: 10.1103/PhysRevB.73.184109.